

Design and Testing of the BionicWingSat in a Zero-g Flight Campaign - A 2U-CubeSat with Deployable, Biologically-Inspired Wings

Martin E. Zander ¹

Institute of Lightweight Systems (formerly Institute of Composite Structures and Adaptive Systems), DLR German Aerospace Center, 38108 Braunschweig, GERMANY, martin.zander@dlr.de

Matthew K. Chamberlain ²

NASA Langley Research Center, Hampton VA 23681, United States of America, matthew.k.chamberlain@nasa.gov

Dominic Jost ³, Daniel Müller ⁴, Niels Hagmeister ⁵, Marco Straubel ⁶

Institute of Lightweight Systems (formerly Institute of Composite Structures and Adaptive Systems), DLR German Aerospace Center, 38108 Braunschweig, GERMANY

In this paper, recent developments in the design, manufacturing, and testing of a novel deployable structure with several potential applications in space will be described. Through a cooperative effort of the German Aerospace Center (DLR) and the National Aeronautics and Space Administration (NASA), a biologically inspired structurally integrated membrane featuring distributed functional elements has been developed and tested in a 2U CubeSat called BionicWingSat. Such a membrane structure could be useful for several applications in which a relatively flat area is desirable such as solar sails, drag sails, or solar shades. For SmallSats and CubeSats, the design proposed also has the desirable property of being self-deploying without the need for powered deployment mechanisms. Building on previous work inspired by the wings of earwigs, the research presented in this paper includes structural design of self-deploying hinges, a survey of various advanced additive layer manufacturing (ALM) methods for making hinges, mechanical characterization of the hinges, and finite element analysis (FEA) of the hinges. In this work, the conflicting goals of maximizing deployed structural stiffness, maximizing deployed area, maximizing stowed packaging efficiency, and maximizing resistance to creep when stowed must be considered. The resulting design concept is a gossamer structure that cannot support its own weight in gravity. For this reason, a focus in this paper is on a parabolic flight test campaign in which 24 fully integrated wings on two BionicWingSats were tested in a microgravity environment. From this test campaign, several lessons were learned regarding the wing design and procedures for carrying out microgravity tests of this manner.

Nomenclature

α_{zMin}	=	minimum angular acceleration
δ_{FzMax}	=	servo angle of HDRM at maximum of exerted force in z-axis
δ_{FzMin}	=	servo angle of HDRM at minimum of exerted force in z-axis
F_{zMax}	=	maximum exerted force in z-axis
F_{zMin}	=	minimum exerted force in z-axis

¹ Principal Investigator of the BionicWingSat project. Research Aerospace Engineer, DLR Institute of Lightweight Systems, Composite Design Department, Lilienthalplatz 7, AIAA Member

² Branch Head, Structural Dynamics Branch (D322), 4 West Taylor St, Mail Stop 230, Senior AIAA Member

³ Student Assistant, DLR Institute of Lightweight Systems, Composite Design Department, Lilienthalplatz 7

⁴ Research Aerospace Engineer, DLR Institute of Lightweight Systems, Composite Design Department, Lilienthalplatz 7

⁵ Student Assistant, DLR Institute of Lightweight Systems, Composite Design Department, Lilienthalplatz 7

⁶ Space Structures and Mechanisms Engineer, DLR Institute of Lightweight Systems, Composite Design Department, Lilienthalplatz 7

t_{FzMin} = time at minimum exerted force in z-axis
 t_{FzMax} = time at maximum exerted force in z-axis

I. Introduction

Membrane dominated structures are generally used in space to collect, reflect, or transmit electromagnetic radiation. Respective examples of such structures include reflectors, solar sails, solar arrays, solar shields, and sun shields. The high cost of launch vehicles and limited space inside launch vehicle shrouds dictate that such structures are generally designed to be lightweight and pack efficiently for launch while still being able to safely and consistently expand in space to achieve the desired geometry. Deployment and maintenance of the desired shape requires stiff structures and mechanisms to motivate the deployment and keep the structure flat, driving up the weight and complexity of the overall system. A simple means of deploying and structurally supporting membrane structures would thus be advantageous, particularly for SmallSat missions which face extreme mass and volume limitations. To provide power using photovoltaic arrays for future SmallSats and CubeSats or other functional areas like solar shades, drag sails or solar sails, or even in low gravity environments as present on Earth's moon, a bioinspired hierarchical structure that can be deployed in space is proposed in this paper.

In previous work done at the National Aeronautics and Space Administration (NASA), an integrated approach to develop a thin-film damage tolerant membrane, incorporating a distributed support structure, was explored using additive layer manufacturing (ALM) [1]. A bio-inspired hierarchical structure was printed on films using additive layer manufacturing to achieve improved tear resistance, areal stiffness and to facilitate membrane deployment. Test results already show this initial work produced higher tear resistance than neat film of equivalent mass. [2, 3] [1, 2] One application of particular interest previously was in power generation. If high packing efficiencies can be achieved using this integrated structural membrane approach, then larger photovoltaic (PV) arrays can be stowed in smaller spacecraft. Possible future applications for such deployable structural membrane systems are the PV arrays needed for solar electric propulsion (SEP) for beyond Earth orbit, large PV arrays on very small commercial spacecraft like Cubesats and Smallsats or even large PV arrays on crewed spacecraft such as the Orion crew capsule.

The work presented in this paper was carried out by the German Space Agency (DLR) and NASA based on a vision for expanding the usefulness of the simple self-deploying biologically inspired membrane developed previously. While the focus in previous work was on power generation, such a light, large membrane structures can also be used for drag sails as shown in Fig. 1, solar shades, reflectors or other functional areas. Drag sails have gained greater importance in the field of CubeSats with the introduction of a new United States Federal Communications Commission (FCC) rule requiring that all satellites in low earth orbit be deorbited within five years after the end of a mission [4]. For this reason, the new advanced self-deploying membrane structure described in this work was designed to be incorporated into a 2U CubeSat form factor for testing in a microgravity environment as if it were a functional drag sail. The development of this BioWingSat, its construction, and testing, are also discussed in this paper.

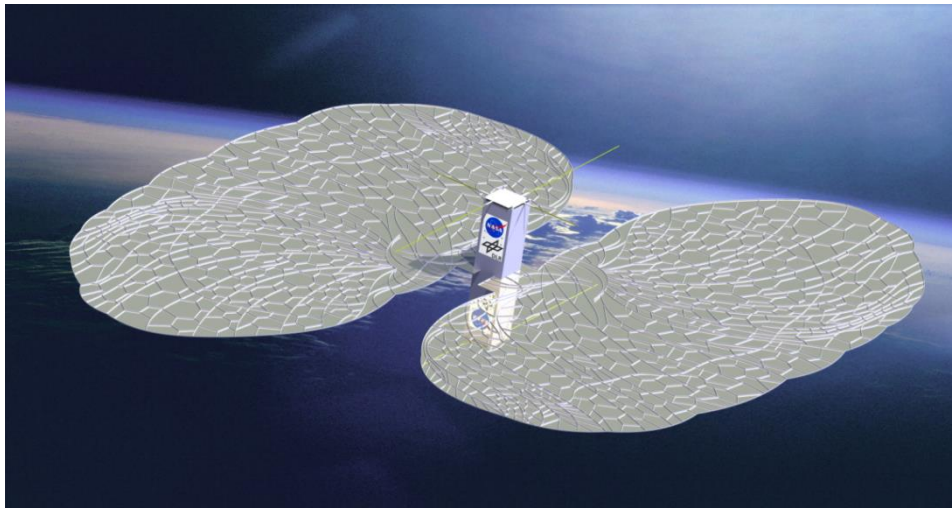


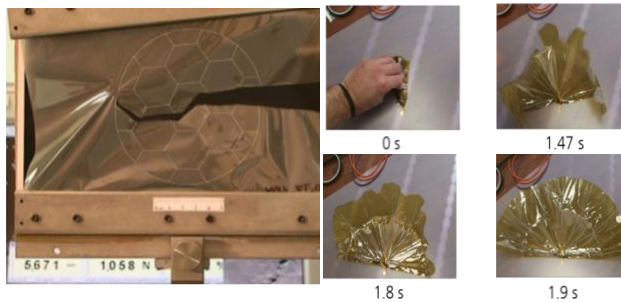
Fig. 1 Artistic impression of the BionicWingSat in space (3 U CubeSat version).

The paper includes five sections describing the process of designing, building, and testing prototype drag sails in microgravity. In Section II, the current state of the art in deployable membrane structures is discussed. In Section III, the process of abstracting earwig wing hinges into a shape that can be used repeatedly and manufactured using ALM techniques is described. Numerous manufacturing techniques and materials were analyzed and tested before identifying a final design that could be built into the hierarchical wing shape. In Section III, the BionicWingSat CubeSat and experimental design is

described. The 2U CubeSat was designed to be agnostic towards wing design, simply providing a robust platform that could be attached to a rigid surface or allowed to float freely in microgravity during deployment. In Section IV, the results of the microgravity experiments are shared, including accelerometer measurements meant to characterize the stability of the CubeSat during deployment as well as qualitative observations of the performance of the various wing pairs. Finally, in Section V, some conclusions on the usefulness of the integrated structural membrane are shared, as are ideas for future research.

II. Current State of the Art in Deployable Membrane Space Structures

As discussed in previous work, [2] nature provides numerous examples of durable membrane structures, from leaves on plants to the wings of bats and insects. The goal in developing the wings for BioWingSat was to include four key functions: enabling folding, allowing self-deployment, providing rip-stop (as previously demonstrated in [2, 3], and exhibiting structural stiffness when deployed. Such structures are seen in nature in the wings of insects such as dragonflies, beetles and other insects [5]. The specific inspiration for the work presented here is the hind wing of the earwig (Dermaptera) due to its incorporation of all four desirable functions [6]. One particularly attractive feature of earwig wings is their 18:1 packing ratio, which is one of the highest values seen in nature [6]. The wing is also stable in both a packed and deployed state, requiring only a small initiation force to self-deploy or re-fold the rest of the way. The structural elements that make up an earwig wing can be classified as belonging to four groups: stiffening veins, foldable elastic hinges, rip-stop structure, and plain membrane, as analyzed in [6]. These elements are repeated in a hierarchical structure to produce a damage-tolerant wing capable of self-deploying repeatedly. Of these, the one most crucial element that is the focus of the work in this paper is the elastic hinges, which provide joints at which the structure can be folded while storing enough energy to allow the wings to be self-deployed later. These hinges were the focus of some previous work [5] using fused deposition method (FDM) structures glued down to Kapton⁷ film as shown in Fig. 2. In the work described here, such structures are approached anew with the goal of using them repeatedly in a hierarchy to build a simple version of the earwig wing as a drag sail. This approach will aim for a lower level of detail than is suggested by Faber, et al [7] in the hope of eventually using the abstracted deployment mechanisms at increasing scales.



(a) Rip-stop test with structure specimens FDM-printed directly on a membrane [2]

(b) Simple deployment test with FDM printed structure bonded on a membrane [3]

Fig. 2 Baseline principles and previous investigations.

In recent decades, deployed membrane structures have seen increased use in space, most prominently as the basis for lightweight solar arrays that package efficiently. The most prominent examples of tensioned membrane solar arrays are the original z-folded arrays used on the International Space Station (ISS) which were deployed and tensioned using a central truss delivered from a large cannister [8]. The power of those original arrays is to be supplemented with a newer generation of high-efficiency Roll-Out Solar Arrays (ROSA) that also feature a tensioned membrane [9]. Both original and supplemental arrays are shown in Fig. 3. Similarly, the Ultraflex family of lightweight solar arrays used on Cygnus spacecraft and two Mars landers feature wedge-shaped sections of photovoltaics mounted onto a section of tensioned membrane [10]. The LISA-T also features a parasol-shaped tensioned membrane with thin solar cells [11].

⁷ Any mention of a vendor or product does not imply the endorsement of that vendor or product by the authors. Any mention is primarily for clarity and reproducibility.

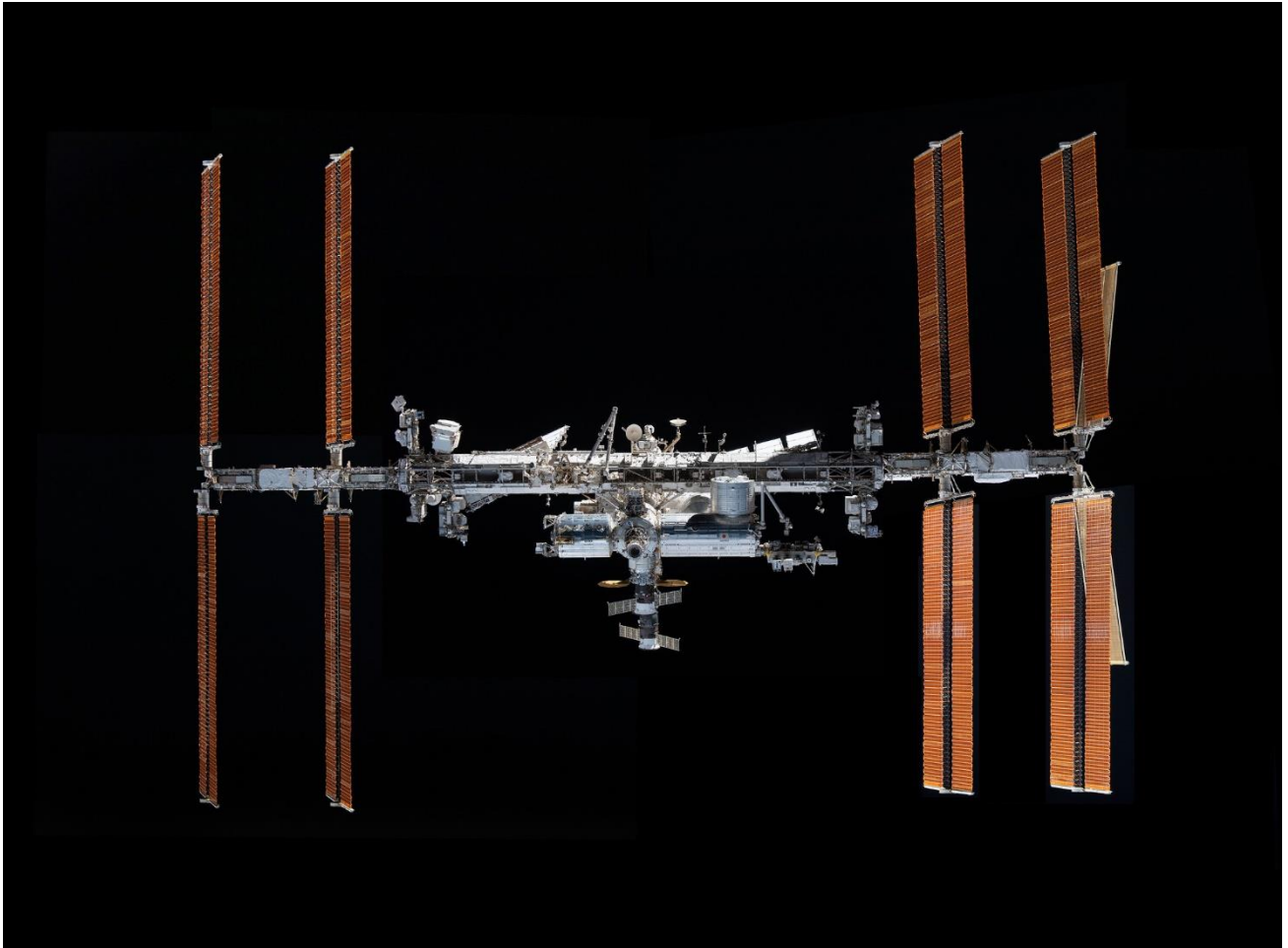


Fig. 3 The ISS shown with its original solar arrays and newer ROSA arrays (Source: NASA).

Two other types of space mission that require lightweight tensioned membranes are solar sails, which utilize solar radiation pressure for propulsion and drag sails that are meant to deorbit payloads by generating atmospheric drag. Solar sail spacecraft like NanoSail-D [12], Lightsail-2 [13], Near-Earth Asteroid Scout [14], Advanced Composite Solar Sail System (ACS3) [15], and Solar Cruiser [16] all feature a reflective metallic membrane that is both deployed and tensioned by separate booms that take up valuable space and require powered deployment systems. A notable exception to this design trend in solar sails is the Ikaros solar sail [17] developed by the Japanese Aerospace Exploration Agency (JAXA), which used spinning motion to both deploy and maintain the stability of its membrane [18]. Numerous drag sail concepts have been proposed including DeorbitSail [19] (shown in Fig. 4) and ROC-FALL [20]. All drag sails consist of a deployment system to extend a tensioned membrane that can generate increased atmospheric drag.



Fig. 4 Functional model of DeorbitSail drag sail (Source: DLR).

The James Webb Space Telescope (JWST) is perhaps the most famous single space mission to make use of large, tensioned membranes. In the case of the JWST, the underside of the spacecraft consisted of five separate layers of quilted Kapton the size of a tennis court that were deployed and tensioned with booms and stainless steel catenaries. [21]

One element in common with all the examples of deployed membrane space structures shared in the previous paragraph is the need for a separate mechanism for deployment and tensioning apart from the membrane that is actually providing the service needed by the spacecraft. Often these mechanisms are not needed after deployment, adding to the mass of the spacecraft but providing no value later in a mission. These added masses are frequently present regardless of whether the membrane is providing space for photovoltaics, a thermal barrier, or a reflective surface for solar radiation pressure-based propulsion. The mechanism may be a literal machine in the case of a boom deployment system or an impulse as in the case of a spacecraft like Ikaros which requires spin to deploy and stay stable. The goal in this work is to integrate the structure and membrane with the eventual goal of producing a more efficient overall spacecraft by packing the membrane and mechanism more efficiently than can be achieved when they are separate entities.

III. Wing Design and Characterization

The design, modeling, and testing of the biologically inspired wings are described in this section. Utilizing a hierarchical plan and building on previous research, candidate wing hinges were designed, parameterized, manufactured, and tested. Surveys of available ALM materials were conducted, and finally a scheme for the overall assembly of the wing was identified.

A. Membrane design and structural elements

Abstracting from previous work on earwigs [1, 4-7], several commonly reused hinge geometries were identified and designed in computer-aided design software (CAD) to create candidate hinges (shown in Fig. 5) that could be tested along with a simpler rectangular-shaped hinge shown in Fig. 6. Each design was parameterized so that it could be easily and quickly scaled based on simple proof-of-concept bending and storage tests. ALM techniques allowed rapid iteration so that multiple generations could be designed, manufactured, and tested in one day. In this way, it was discovered that some hinge geometries intended for one purpose might serve well in other roles based on the materials and design parameters selected. For instance, some hinges were abstracted from places in earwig wings where they provided out-of-plane bending but when manufactured out of thinner material capable of taking more strain, they provided good deployment torque when subjected to in-plane bending or twist. By changing material properties as the prototypes were created, a search for appropriate materials to make these hinges was conducted in parallel with the design effort. This search is described in more detail in Subsection D.

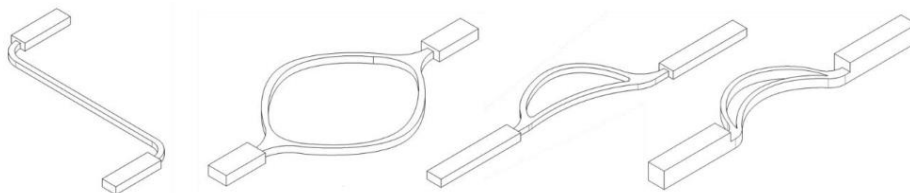


Fig. 5 Candidate hinge designs derived from earwig wings including the O-Hinge (second from left).

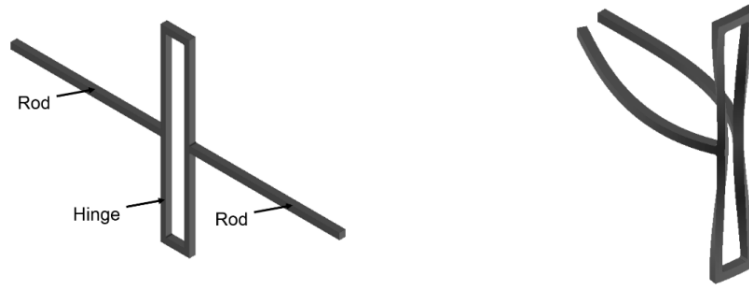


Fig. 6 Original rectangular hinge design.

Originally, the drag sail wings were meant to be hierarchically ordered using various hinges idealized and optimized from earwig wings. Eventually, this idea was simplified to the structure as presented in Fig. 7 and a folding scheme shown in Fig. 8. The wings are divided evenly into sections of a circle comprising 35 degrees of an arc. Each section has two lines of hinges with smaller hinges closer to the hub at the center of the spacecraft. Each section is bordered by radial stiffeners. In this way, the wing can be fan-folded at radial locations where the hinges line up as shown in Fig. 8 (b). The fan-folded wing can then be wrapped around the central hub of the spacecraft. The radial stiffeners wrapped around the hub provide the initial kick from their stored strain energy to begin deployment while the circumferentially arranged lines of oval hinges provide final motivation to spread the wing and stiffen it when deployed. The final size of the wing and its sections was determined based on the ability to store two wings and the central hub within the 1U (10 x 10 x 10 cm) space allotted to them in the BioWingSat.

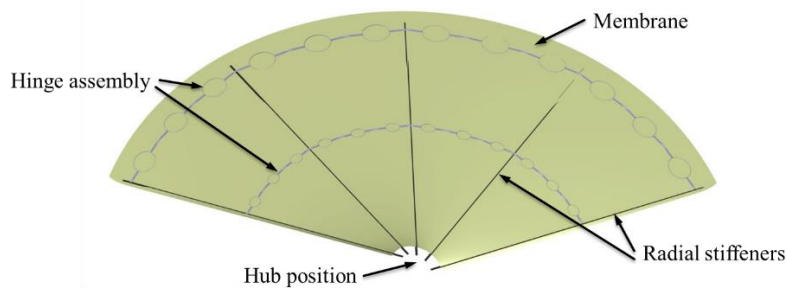


Fig. 7. Main components of an assembled wing.

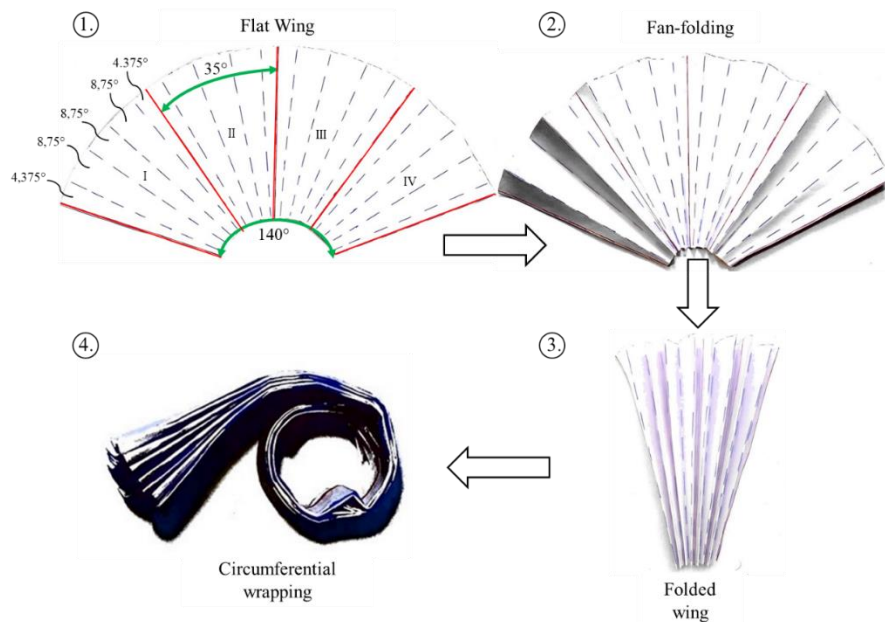


Fig. 8 Wing folding scheme: z-folding and subsequent wrapping around a hub.

B. Modeling

Parameterized models of the hinges were created in CAD so that their geometry could be imported into finite element analysis (FEA) software for full analysis of the folding process. The geometric parameters for the rectangular torsion hinge and the boundary conditions applied to the model are shown in Fig. 9 (a). The parameters adjusted in this torsion hinge were the length, width, and height of each element of the part. Later models derived from the earwig such as the O-Hinge also included parameters like curve radii as parameters. In each analysis, boundary conditions were applied so that one leg of the hinge was fixed while the other underwent prescribed displacement until the hinge was fully folded. These simulations yielded large deformations that required careful selection of the finite element mesh to achieve convergence. The equivalent von Mises stress on the torsion hinge geometry during its folding procedure is shown in Fig. 9 (b). The central elements experiencing the largest deformations are also subject to the largest stresses. The hinge designs were adjusted over time with the goal of finding a geometry able to distribute the stress such that no permanent deformation occurs in the material during the folding procedure and the whole deformation energy can be used in a later deployment of the structure.

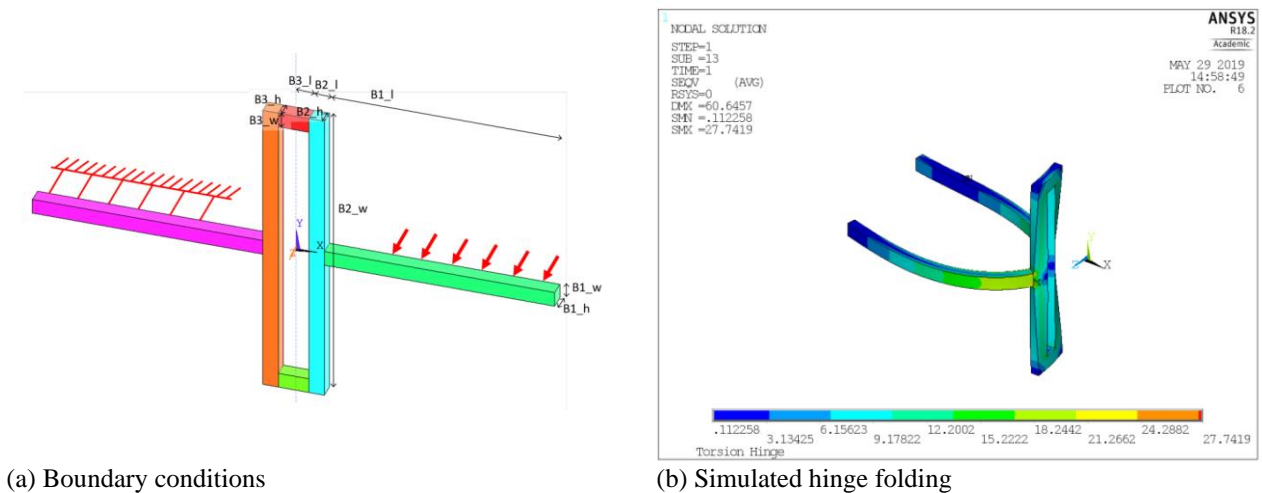


Fig. 9 Modeling and simulation of exemplary folding hinge elements.

Eventually, a geometry was found for the hinge design that was used in the BioWingSat through a sensitivity study in combination with a finite element simulation in which hinge parameters of several hinge types were varied. The finite element solution of the folding sequence of this hinge is shown in Fig. 10 edge-on starting from a flat hinge (top left) through different stages of folding until a fully folded structure (lower right) that resulted in acceptable stress and strain values even at full closure. The center part of the O-Hinge has a large in-plane and out-of-plane displacement, which must be considered when constraining the hinge's displacement on a membrane as described in subsection D. The time indicated in each frame of Fig. 10 corresponds to the location of the testing mechanism during the mechanical characterization tests that are explained in subsection C.

By varying the design parameters, as presented exemplary for an O-hinge in Fig. 11, maximum stresses, strains and reaction forces were calculated and tracked throughout the simulations. The results of the sensitivity analysis, as shown exemplary in Fig. 12, indicated that changing the thickness, t , of the joint had the largest influence on the reaction force and the von Mises stress. Other parameters did not show such a strong influence. Consequently, thickening the joint leads to both an increase in the reaction force as well as the mechanical stress. Hence, a trade-off between a stress not too large to induce mechanical deformation but leading to a reaction force as large as possible had to be taken.

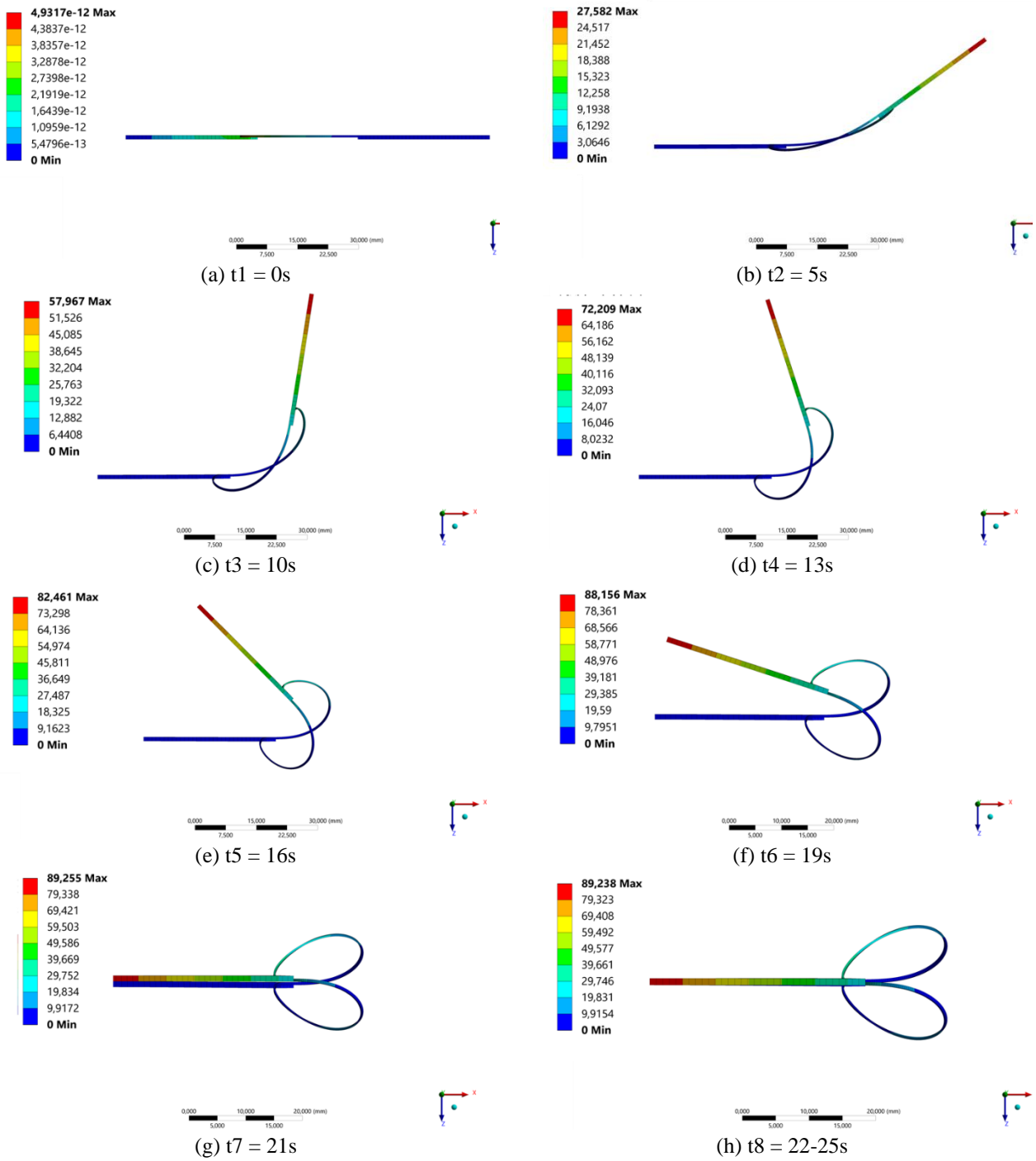


Fig. 10 Full folding simulation of a candidate O-hinge design.

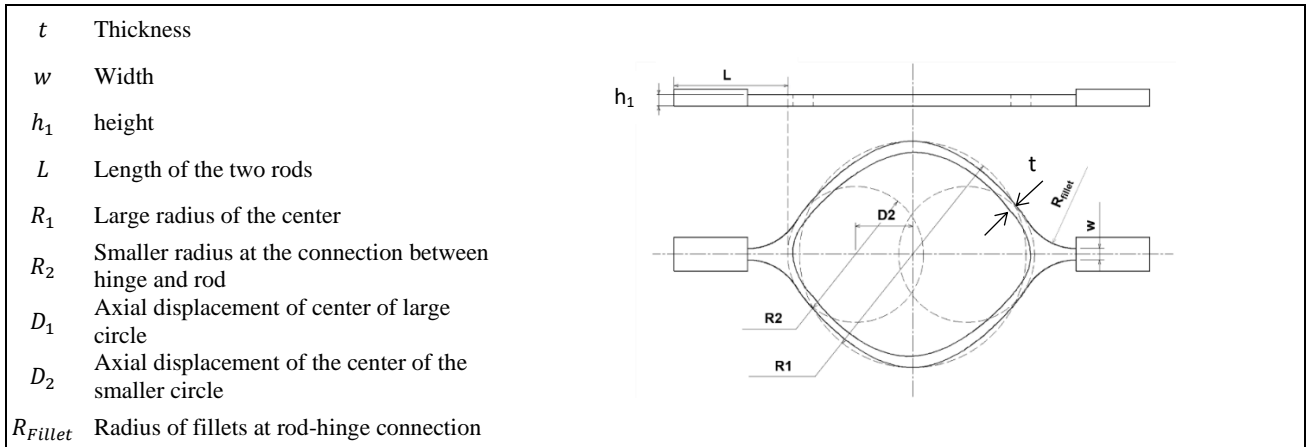


Fig. 11. Design parameters varied for sensitivity analysis of an O-hinge.

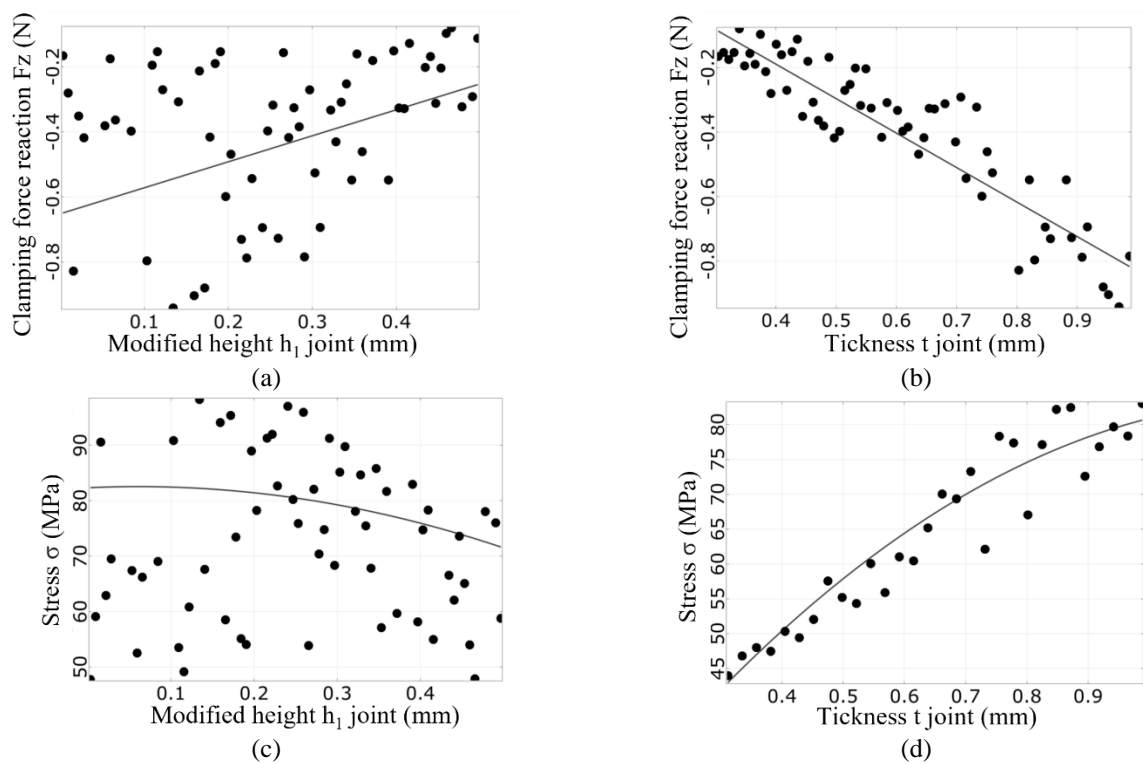
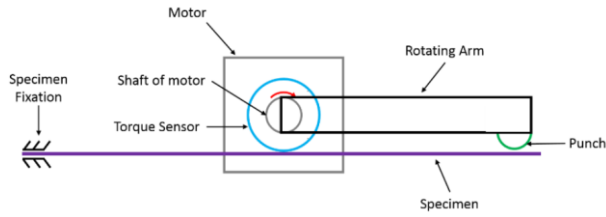


Fig. 12 Sensitivity analysis with linear regressions of folding reaction force (a), (b) and stress (c), (d) on the example of O-Hinge design parameters.

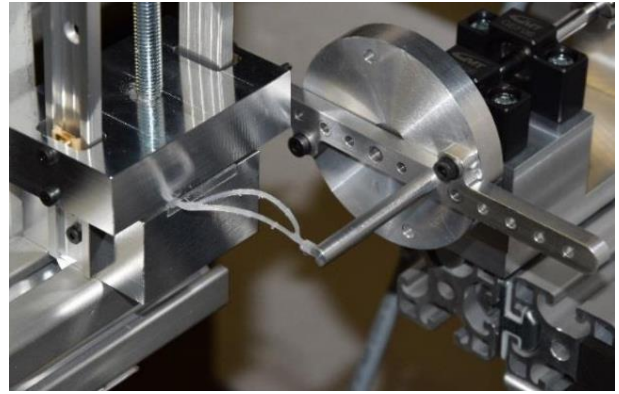
C. Mechanical characterization

To validate the FEA results presented in the previous subsection, a customized hinge test apparatus was designed and used to characterize the bending characteristics of each candidate hinge. In this subsection, the design of the testing apparatus is described, as are the results of the test of several combinations of hinge designs with different materials.

A diagram of the hinge test apparatus is shown in Fig. 13 (a). The specimen being tested is fixed at one end to be consistent with the analyses described in subsection B. The free end of the specimen is displaced by a rotating arm with a round contact that does not apply tension to the hinge. The setup is adaptable to different specimen sizes, as the position of the punch on the rotating arm as well as the specimen fixation can be moved. It is important that the specimen is placed such that its center is in the axis of the rotating shaft. This alignment ensures a central bending of the specimen. A torque sensor measures the reaction torque on the rotating arm while folding the specimen. The final version of the test apparatus with a specimen fixed and ready to be folded is shown in Fig. 13 (b).



(a) Hinge folding test setup



(b) Hinge in test rack

Fig. 13 Hinge mechanical test apparatus.

As an example of the results that can be generated using this apparatus, the reaction forces in x-, y-, and z-direction, as well as the total force during the folding procedure are shown for two different O-hinge designs in Fig. 14. At time zero, the folding procedure has been initiated and after 22–25 seconds the specimens have been fully folded. The solid and dotted lines are results from the O-hinges with diameters of 28 mm and 41 mm, respectively. The total reaction force is strongly dependent on the diameter of the O-hinge, as the final force increased by more than a factor two, whereas the diameter was only increased by about 50%.

Aside from checking values like bending force against their predicted values from FEA, the mechanical testing provided an opportunity to check the ability of hinge designs to restore themselves to their original shape after deformation and storage in the folded position over different lengths of time. Candidate hinges were loaded into the testing apparatus, folded, and left to sit to simulate storage. Hinges were examined after unloading to confirm their ability to completely recover their original unfolded shape. In this way, creep in the hinge material was avoided. The overall design of the wing (explained in subsection D) also provided a means of eliminating deflections that induced creep.

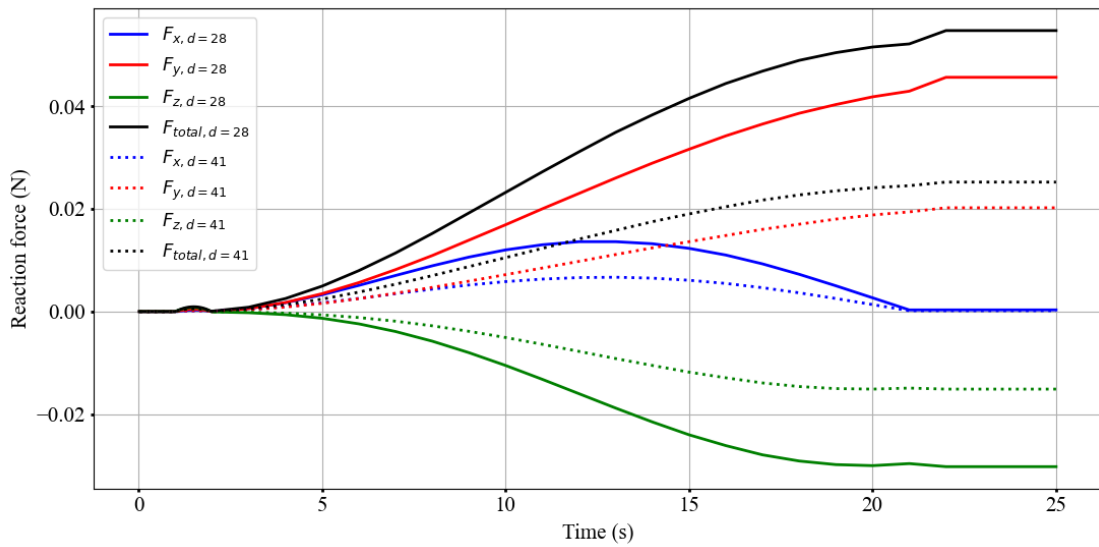


Fig. 14 Reaction force time histories for various hinge designs.

D. Manufacturing approach

Design of the BionicWingSat hinges occurred in parallel with a study of manufacturing techniques. Additive layer manufacturing was identified early on as being advantageous in this project due the ease with which updated hinge designs could be manufactured and tested. Therefore, the search for an ideal manufacturing technique was focused on finding the best ALM machine, machine settings, structural material, and means of adhering that material to the membrane.

Five different hobby-grade and professional-quality ALM machines were utilized to manufacture simple sample hinges out of single materials. A small sample of the hinge samples made for this purpose is shown in Fig. 15. Early on, simple folding tests were used as a means to eliminate materials and designs that could not sustain folding without plastic deformation or which exhibited creep when stored closed. Evidence of this testing is seen in the samples in both Fig. 15 and Fig. 16. Sample hinges made of Acrylonitrile butadiene styrene (ABS), polyactic acid (PLA), polyvinyl alcohol (PVA), ULTEM brand polyetherimide, thermoplastic polyurethane (TPU), high impact polystyrene (HIPS), and various types of Nylon were all tested in this phase.

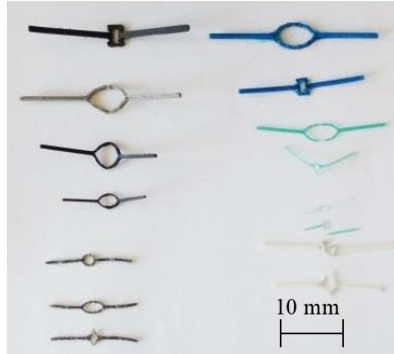


Fig. 15 A selection of single samples from machine and material surveys.

Other samples were made with combinations of materials with the intent of using those that were softer and more capable of absorbing greater strain to permit folding while using stiffer materials to give the deployed wings some rigidity. Samples of hinges made with combinations of materials are shown in Fig. 16. This idea was ultimately dropped due to challenges in maintaining the bond between dissimilar materials and the inherent thickness that the combinations created.

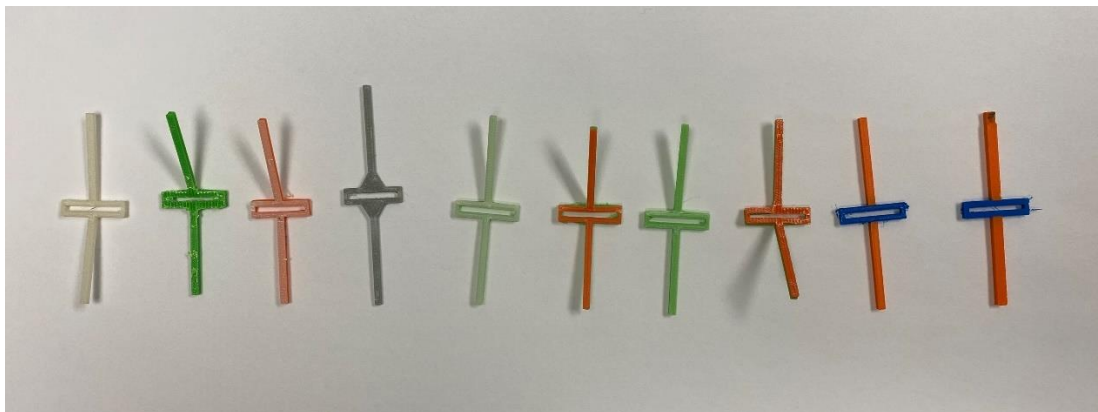


Fig. 16 Multi-material hinge samples.

Nylon was selected for the hinge materials due to its flexibility and toughness. Sample hinges made with this material also demonstrated an ability to completely fold, stay in storage, and return to their original flat shape. The available ALM machines were also capable of making delicate structures like the prototype hinges shown in Fig. 17 out of Nylon at various scales. The final “Infinity Hinge” design and the curved members used to connect them are shown in Fig. 18. The “O-Hinge” had originally been conceived as being lined up circumferentially as shown in Fig. 7. Hands-on experimentation with fan-folding and rolling hinges aligned in this manner showed that the hinges needed an ability to shear about the circumferential lines. Offsetting the hinges at angles in the “Infinity Hinge” orientation shown in Fig. 18 proved to provide the desired behavior in the wing.

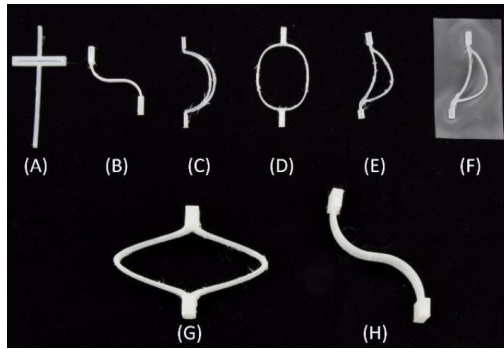


Fig. 17 ALM Nylon hinge variations.

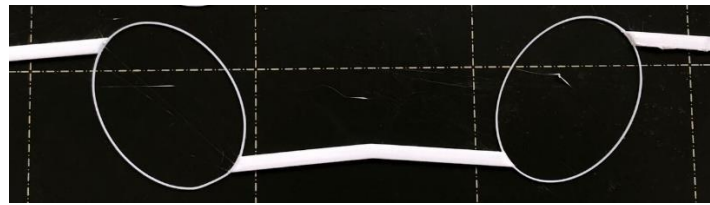


Fig. 18 Hinge segments for flight wings with parameters identified.

Build volume limitations drove some design decisions that were made, including the choice to break the wing structures down into radial stiffening ribs and repeated hinge sections like those shown in Fig. 18. The biggest manufacturing challenge was identifying a means to integrate the structure into the membrane. Initially, the structure was to be printed directly onto the membrane but print quality concerns drove the decision to print the structure separately and attach it to the membrane. Having made this decision, various adhesives were tested but found to either create too much material buildup or to fail in shear during folding. Several alternative approaches to using heat to bond ALM hinges to the membrane were attempted, as shown in Fig. 19. In the end, the approach used in references [8] and [9] and shown in Fig. 19 (d) and Fig. 20 was utilized: a thin sheet of polyester fibers melted between the aluminized Mylar film and the printed Nylon structure.



Fig. 19 Examples of various integration schemes.



Fig. 20 Examples of polyester membrane adherence trials at increasing scales.

Due to limitations in the build volumes of the available ALM machines, a strategy for assembling the additively manufactured hinges hierarchically into the larger wing shape described in Section III also had to be identified. Various strategies were investigated, including heating two butt-joined additively manufactured sections with an iron or heat gun, but the joints between sections proved prone to failure. At small scales, new combinations of ALM materials were also used to combine rigid wing ribs with flexible hinges as shown in Fig. 18. Wings assembled in this manner also failed at the joints. A simpler option had to be adopted in the end. Rigid ribs were combined with flexible ALM hinges using small amounts of Kapton tape and the fused polyester that bound both elements to the membrane. All samples were built with the basic plan shown in Fig. 7 using five carbon fiber reinforced plastic (CFRP) radial stiffeners and either two or three rows of hinge assemblies (cf.) as illustrated schematically in Fig. 21. Some of the wings also feature shorter radial stiffeners or stiffeners with doubled thickness. This feature was added with the goal of increasing deployment forces and achieving greater flatness once deployed. Examples of the six different wing types and the twelve final assembled wing assemblies, are shown in Fig. 22. A schematic overview of the samples and wing types tested is further provided with Table 1. The manufacturing methods discussed here are meant to demonstrate the concept of the integrated structural membrane in a manner that might be achieved later with space-qualified materials.

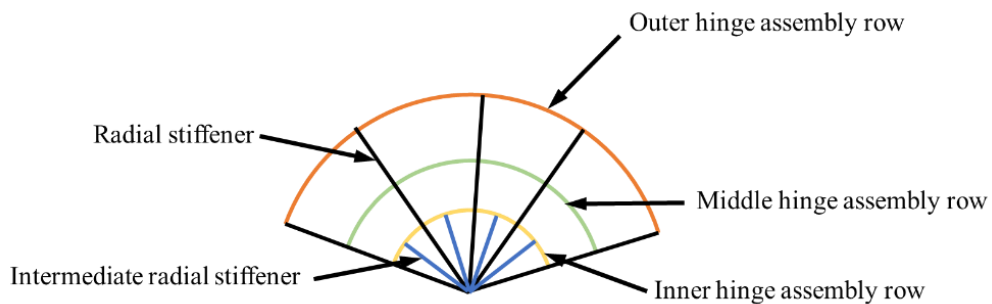


Fig. 21 Scheme of elements varied for the different wing types.

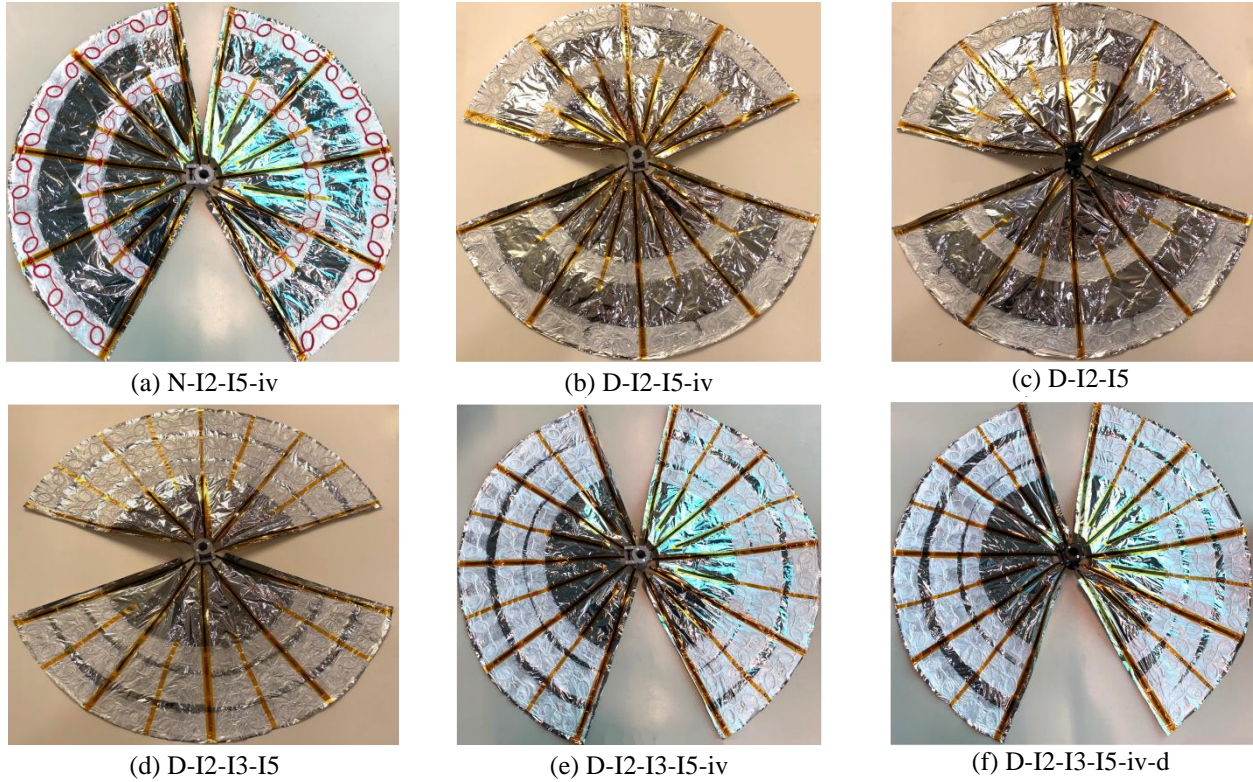


Fig. 22 Six of the assembled BionicWingSat flight wing pairs prior to folding.

IV. BionicWingSat design

One key challenge for any membrane structure optimized for use in space is that it will likely be too weak to support its own weight in gravity. Indeed, the wings designed here were incapable of self-deployment without manual assistance or favorable orientation relative to gravity. For this reason, verification of the function of the wings needed to be carried out in microgravity. In this section, the microgravity experiment designed and carried out to verify wing design is described. The experiment was carried out on a dedicated DLR parabolic flight in July 2021 in Germany and over the Atlantic Ocean near France.

A. Satellite Platform

One of the key design constraints in this work was the restriction of the packaged wing volume to a 1U space in a CubeSat. For this reason and to demonstrate future applicability to SmallSats, the microgravity experiment was designed to mimic a 2U CubeSat with one half of the volume reserved for wing storage and the other half dedicated to electronics, data acquisition, and mechanisms. The design of this satellite can be followed in the images of Fig. 23.

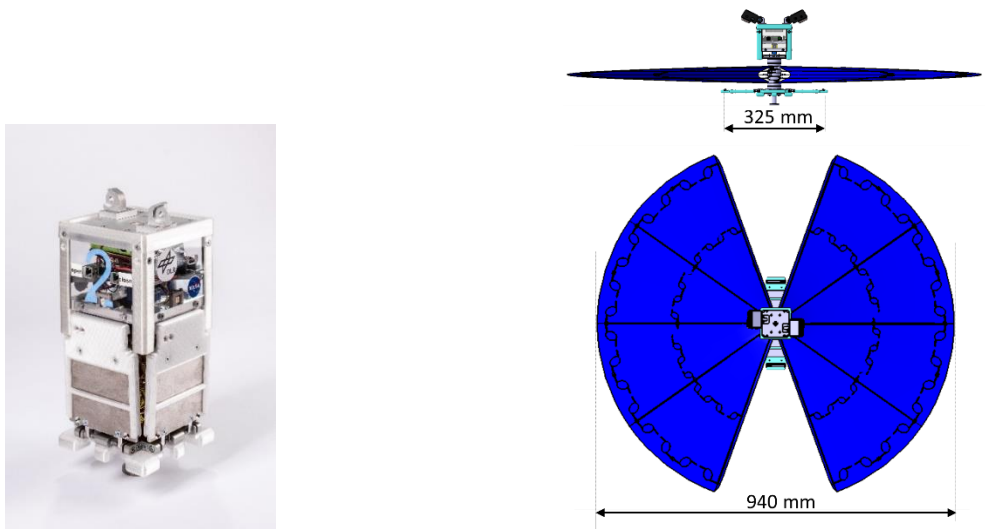
The electronics and mechanism compartment contains the electronics board, a battery pack, a motor, and the mechanism to release the door, as shown in Fig. 23 (a) and Fig. 23 (c). During a wing deployment, the stored wings are released in a separate two seconds after the four doors are unlocked and open. The motion of the door is rapid but damped by an adjustable hinge mechanism so that it takes two seconds to complete. To protect equipment and personnel during experiments the aluminum BionicWingSat main structure is covered with elastic safety bumpers at all sharp edges (see Fig. 23 (a) and Fig. 23 (c)).

The wing compartment contains the two wings and the central hub. Once released, the two wings self-deploy outward in a symmetric circular fashion, reaching a nearly circular overall shape approximately 940 mm in diameter, as depicted in Fig. 23 (b). Once the wings have been deployed in an experiment (as shown in a ground test in Fig. 23 (d)), the wings and its hub can be quickly removed and replaced by a packed wing hub with two stowed and fixed wings. An example of a packed hub is depicted in Fig. 23 (e). The additively manufactured hub connects each radial vein of a wing to the connecting each vein of a wing to the BionicWingSat.

Equipped with a leash for safety purposes, the BionicWingSat was retracted by the operator in the free-floating area during microgravity testing, thus preventing the BionicWingSat from dropping/crashing to the floor at the end of each 0g-phase. After each test run, the packed wings were installed, and the doors were manually closed and locked with onboard switches. The process of refurbishment -including unmounting deployed wings and mounting new packed wings on a hub-takes less than one minute and was performed during the 0g-phase of dedicated parabolas.

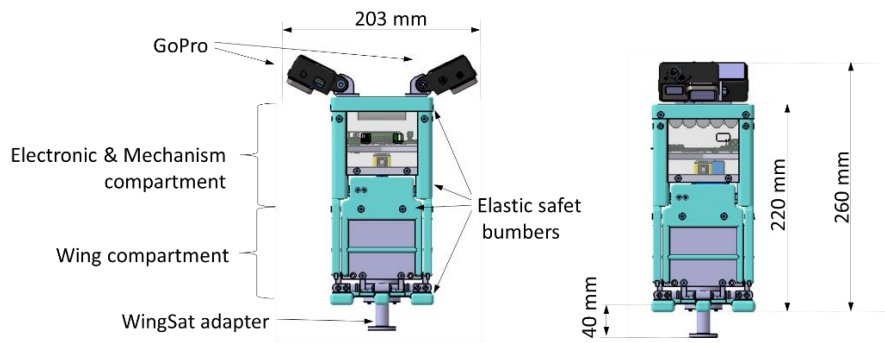
The BionicWingSat is also equipped with an electronic board enabling a wireless control of all functions and hosting a gyroscope sensor, an accelerometer, and LEDs to indicate the status of the systems onboard. It also includes several

switches for manual control e.g., locking, unlocking and turning the power on or off. In addition to the onboard sensors, two small, rugged cameras were mounted on a BionicWingSat for visual documentation of the experiments.

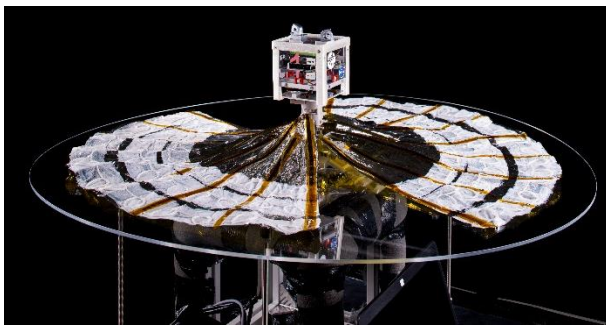


(a) Stowed BionicWingSat (GoPros not displayed)

(b) Deployed BionicWingSat



(c) Main dimensions and compartments



(d) Deployed wings in ground test



(e) Stowed wing hub (lab sample)

Fig. 23 Main features of the BionicWingSat.

B. Microgravity Test Rack

The rack provided a place to mount all the experimental hardware onto the airplane cabin floor during microgravity testing. It holds the data acquisition system (DAQ), a laptop for BionicWingSat and sensor control, a main power switch, and a quick mount adapter for holding the BionicWingSat onto the rack during rack-bound experiments. The rack also housed several sensors including an accelerometer to generate data that could be compared with aircraft motion and a 3-axis force sensor mounted directly below the quick-mount adapter to measure reaction forces of the BionicWingSat. All necessary electrical and power supply components are mounted on a middle plate of the test rack. These main features are illustrated in Fig. 24. The safety screen, as illustrated in Fig. 24 was not used in the flight, as it restrained experiment handling and was judged not to provide any improvement in experiment safety.

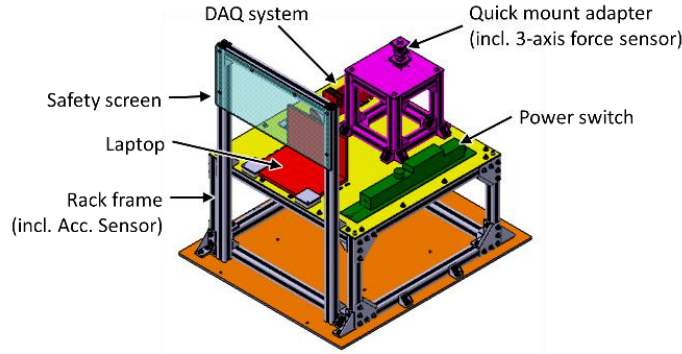


Fig. 24 Main features of test rack.

V. Microgravity Deployment Experiment Procedures

The experiments in the microgravity test campaign were performed in two test configurations: a rack-bound configuration and a free-floating configuration in a dedicated area enclosed by safety nets. The goals were: demonstrating deployment, comparing different wing types, investigating the dynamic behavior caused by deployment, and investigating how flat each of the deployed wings was after deployment. The latter however could only be qualitatively studied, as photogrammetry and image correlation were not applied.

A. Principle and Methodology

1. Test setup:

The BionicWingSat experiments were planned and set up to be tested in two configurations: a rack-bound configuration in which the BionicWingSat is fixed via quick mount to the test rack (see Fig. 25 (a), Fig. 25 (b)); and the free-floating configuration in which the BionicWingSat is freely floating in a dedicated area (see Fig. 25 (c), Fig. 25 (d)). In both configurations the BionicWingSat is remotely controlled from the laptop in the test rack, commanding system activation, door opening and wing release. Moreover, measured sensor data and housekeeping data are fed back live via Bluetooth to the DAQ system into LabView.

Experiments in the rack-bound configuration started with a BionicWingSat mounted to the rack, with closed and locked doors, holding the stowed wings inside, as illustrated in Fig. 25 (a). When the carrier aircraft reached a steady microgravity level the BionicWingSat (as depicted in Fig. 25 (b)) was remotely triggered to open its doors and then release its wings. During deployment, the laptop in combination with a DAQ system acquired sensor data from rack integrated sensors as well as from sensors onboard the BionicWingSat.

In the free-floating configuration deployment experiments were carried out in a dedicated area enclosed by a net. The BionicWingSat was held by an operator and placed in the middle of the area once a steady microgravity was achieved and released to float freely, while the doors were still closed, as illustrated in Fig. 25 (c). Door opening and wing deployment were then initiated as illustrated in Fig. 25 (d).

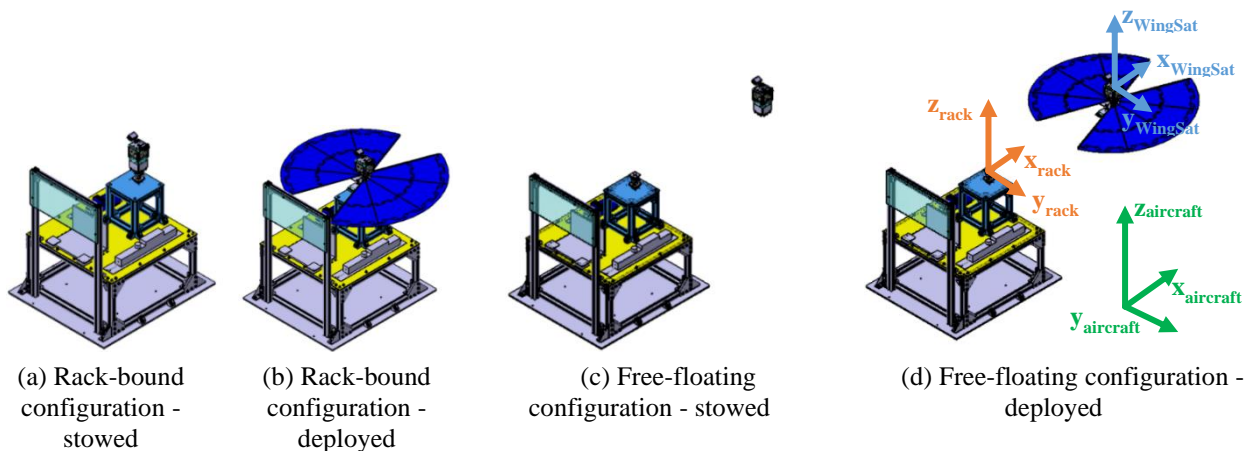
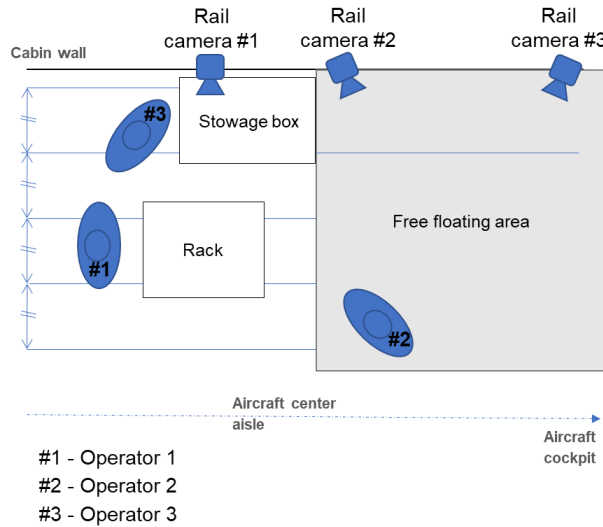


Fig. 25. Test configurations and aligned test coordinate systems: BionicWingSat (blue), rack (orange), aircraft (green).

The overall test setup in the aircraft cabin, with the test rack and free-floating area displayed, is illustrated in Fig. 26 (a). To carry out the planned twelve deployment experiments in the two configurations with twelve different samples, a storage box was used and placed close to the rack for easy access (see Fig. 26 (a)). The box contained all prepared samples (stowed wings on exchangeable hubs) prior to use as well as the wing sets that had been deployed already, both BionicWingSats, and some tools. To safely perform all tasks of the experiment including refurbishment, three crew members were necessary. The first crew member was operating the rack and DAQ system, the second was responsible for refurbishment near the storage box, while the third was operating the BionicWingSats in the free-floating area, as illustrated in Fig. 26 (a). In addition to the two cameras mounted on a BionicWingSat, three cameras mounted on rails of the aircraft cabin were used to monitor the deployment experiments from a third person view (see Fig. 26 (a)). Examples of the rack-bound and free-floating experiments performed during 0g-phase are shown in the images (b) and (c) of Fig. 26, respectively.



(a) Test setup in airplane



(b) Testing in rack-bound configuration



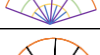
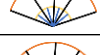
(c) Testing in free-floating configuration

Fig. 26. Test configurations of during in-flight testing (0g-phase).

2. Test procedure

The plan for the use of each test article and the parabola in which it was used is shown in Table 1. The rack-bound experiments were performed within the first eleven parabolas. Note that the experiment in parabola #9, with sample #F, had to be repeated in parabola #11, due to a stalled unlocking. The parabolas in between were used for refurbishment of the BionicWingSat and for re-equipping it with a new, still stowed, wing module (hub with stowed wings). The tested and deployed wings including its hub were stowed away as soon as they are removed from the BionicWingSat. In the scheduled breaks within the overall flight refurbishment, an exchange of camera batteries and back-stowing of the deployed wing modules was performed. After finishing the last experiment in parabola #23, all samples, BionicWingSats and tools were stowed away in the stowage box.

Table 1. Test plan of realized experiments during flight.

# Parabola	# Deployment	# Sample	Wing type	Wing type	Test type
1	1	A	D-I2-I5-iv		Rack
2	2	B	D-I2-I5		Rack
3-4	Refurbishment				
5	3	C	D-I2-I3-I5-iv		Rack
Break 5 min - refurbishment of WingSat 2					
6	4	D	D-I2-I3-I5		Rack
7	5	E	N-I2-I5-iv		Rack
8	Refurbishment				
9	6	F	D-I2-I3-I5-iv-d		Rack
10	Refurbishment				
Break 5 min - refurbishment of WingSat 2					
11	7	F	D-I2-I3-I5-iv-d		Rack
12	8	G	D-I2-I5-iv		Free
13-14	Refurbishment				
15	9	H	D-I2-I5		Free
Break 8 min - refurbishment					
16	10	I	D-I2-I5-iv		Free
17	11	J	D-I2-I5		Free
18-20	Refurbishment				
Break 5 min					
21	12	L	D-I2-I5-iv		Free
22	Refurbishment				
23	13	K	N-I2-I5-iv		Free

The major steps of the test procedure for experiments in the rack-mounted configuration were as follows:

1. BionicWingSat is fixed to the test rack by quick mount, cameras are activated
2. BionicWingSat is activated, Bluetooth connection is established
3. Wait for steady 0g-phase
4. BionicWingSat is remotely triggered from LabView (laptop) to unlock its four doors, triggering recording/transmission of sensor data at the same time
5. With a 4 s delay wing release is automatically initiated, immediately followed by their autonomous self-deployment
6. In the following 1g phase, the BionicWingSat is then replaced by the second prepared BionicWingSat that is still locked (closed doors, stowed wings)
7. The used BionicWingSat with its deployed wings is refurbished and equipped in a quick-change procedure with a new, still stowed, wing hub, holding two stowed wings
8. The deployed wings and hub are stored away in the stowage box
9. Repeat the process

Several dry runs on ground, in the aircraft cabin, had been performed for both configuration prior to the flight, as depicted for the rack-bound configuration in the images of Fig. 27.

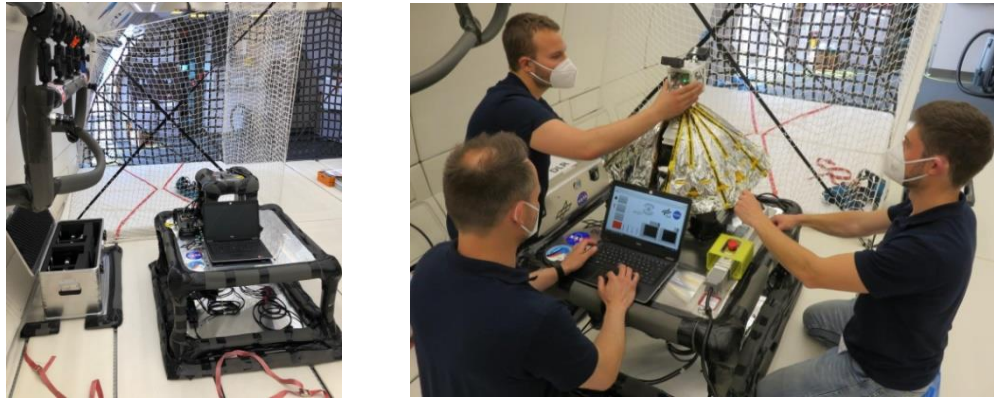


Fig. 27. Test run on ground in airplane cabin prior to flight.

The major steps of the test procedure for experiments in the free-floating configuration were as follows:

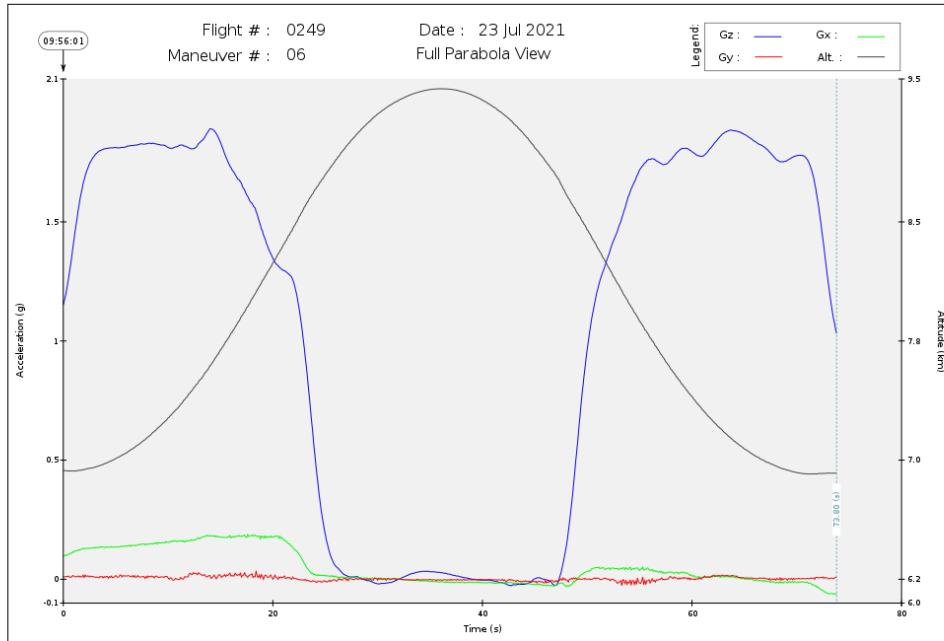
1. BionicWingSat is activated and held in the center of the free-floating area by operator #2 (as shown in Fig. 26 (a))
2. Bluetooth connection between laptop and BionicWingSat is established
3. Wait for steady 0g-phase
4. BionicWingSat is remotely triggered from laptop to unlock its four doors, triggering recording/transmission of sensor data at the same time
5. With a 4 s delay wing release is automatically initiated, immediately followed by their autonomous self-deployment
6. BionicWingSat is retracted towards operator #2 using the attached leash and captured, while still in 0g-phase
7. In the following 1g phase, the BionicWingSat is then replaced by the second prepared BionicWingSat that is still locked (closed doors, stowed wings)
8. The already tested BionicWingSat with its deployed wings is refurbished and equipped in a quick-change procedure with a new, still stowed, wing hub, holding two stowed wings
9. The deployed wings and hub are stored away in the stowage box
10. Repeat the process

B. Experimental results

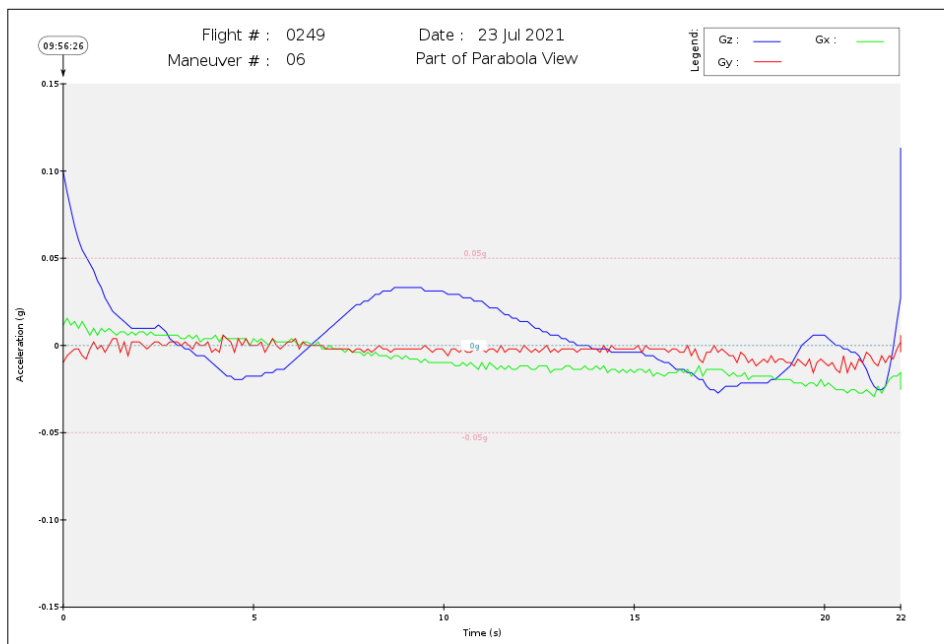
The results of each of the twelve microgravity experiments are described in this subsection. For each parabola and sample onboard sensor data of BionicWingSat and rack were analyzed along with the video footage taken. Each of the test configurations provided different sets of useful data. The rack-bound configuration delivered results for the door opening dynamics and forces, while the free-floating configuration primarily provided results on wing deployment and the associated dynamic responses of the satellite.

In general, the quality of the microgravity environment produced by the aircraft parabolic maneuver was good. Microgravity with $< \pm 0.03$ g in all axes was provided for about 20 s out of each parabola. The accelerometer data from the aircraft for parabola #6 is presented in Fig. 28 (a) with a focus on the 20 s of microgravity in the middle of the parabola in Fig. 28 (b). The residual gravity, while small, was enough to cause the BioWingSat to drift when released on the plane, sometimes resulting in it impacting the net enclosing the experimental area for safety.

More physical interactions between the BionicWingSat, rack and aircraft were visible in the rack-bound configuration. A dynamic excitation about all axes of the mounted BionicWingSat was observed during these parabolas, caused by the aircraft engines, transmitted thru the floor into the fixed rack. This is reflected in the results discussed in the following paragraphs, as vibration amplitudes exceed amplitudes e.g. of wing deployment, making some of the sensor data unusable.



(a)



(b)

Fig. 28. Measured airplane accelerations: (a) for the entire 70 s parabolic maneuver, (b) during the 20 s microgravity phase in parabola #6, vertical z-axis (blue), lateral y-axis (red), axial x-axis (green).

1. Rack-bound configuration

The rack-bound configuration was the first to be tested. All six wing types were deployed each in separate parabolas. Although all test runs are started and ended in the 0g-phase, strong vibrations were induced by the airplane during testing as well as some data loss of the DAQ system occurred. Thus, only two of six test runs generated analyzable sensor data output. Nevertheless, all test runs delivered video footage of deployment behavior. The most valuable results from the rack-bound tests are the forces measured at the base of the fixed BionicWingSat, especially the forces measured in the z-axis of the BionicWingSat. In Fig. 29c, the graphs of the two analyzable test runs are showing the exerted force in z-axis F_z over time. To help relate the loads measured with the state of the wings, the angle of the servo motor of the release mechanism is also shown. The steps of the unlock and release sequence are marked with numbers one to six, as shown in the right image of Fig. 29. Starting the test run with the BionicWingSat mounted to the rack, the doors were locked and the

packaged wings were tightly held in place. Even in this phase, the airplane vibrations are visible in the graph as well as in the video footage. The sequence started at mark ① with the doors opening, initiated by turning the release mechanism from 90° to about 0°. At mark ② the door unlocking process was completed and the doors began to swing open. The swinging is visible in the rising F_z amplitude in upwards (positive) direction, as the lowering doors were pushing the BionicWingSat upwards. The decrease of amplitude marks the doors reaching their end stop with a smaller subsequent bounce backward.

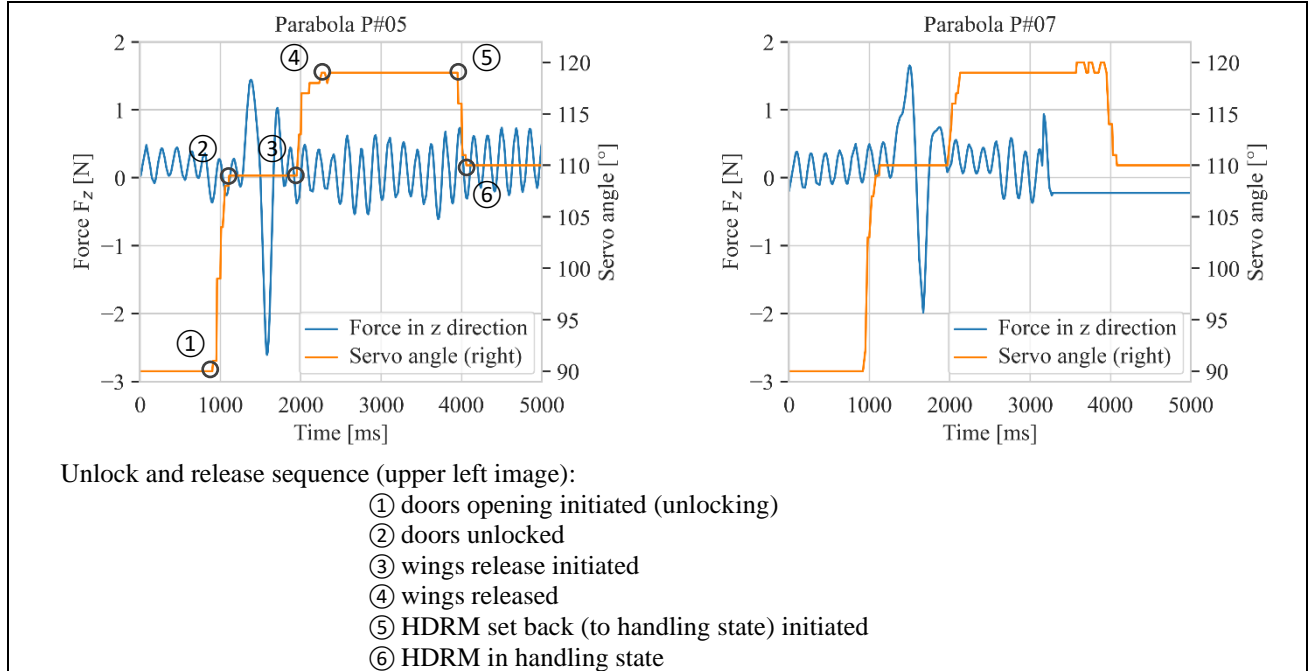


Fig. 29. Forces in z-axis exerted by the BionicWingSat doors during rack-bound deployment tests.

In Table 2, the detected maxima and minima forces with F_{zMax} and F_{zMin} are provided along with the time at event and the corresponding servo angle. Here the first peaks (F_{zMax}) are between 1.4 N and 1.7 N, while the second peaks (F_{zMax}) are between -2.6 N and 2.0 N. The force exerted is thus repeatable. After about two seconds, the wing release was initiated (at mark ③ in Fig. 29) by increasing the servo angle, δ , to 117°. At mark ④ the wings were released starting their self-deployment. This however is not noticeable in the force amplitude as the vibrations overlay the very small forces exerted by the wings. Nevertheless, only very small forces in z-direction were expected due to the radial wing deployment. Each test run was ended when the hold-down release mechanism was set back to the handling state starting at mark ⑤ and end at mark ⑥ at about 110° servo angle. In the handling state, the wing sample could be replaced with an undeployed one for the next test run, as described previously. The data gathered demonstrates that the door opening has an impact on the dynamics of the BionicWingSat itself. This outcome will be compared to results of a ground test campaign in a later publication. This data may be valuable in predicting induced motion for a satellite with similar wing systems.

Table 2. Maximum and minimum forces in z-axis of the rack-mounted BionicWingSat.

Parabola	Wing sample type	t_{FzMax} [ms]	F_{zMax} [N]	δ_{FMax} [°]	t_{FzMin} [ms]	F_{zMin} [N]	δ_{FMin} [°]
P#05	D-I2-I3-I5-iv	1380	1.4	109	1580	-2.6	109
P#07	N-I2-I5-iv	1500	1.7	110	1670	-2.0	110

2. Free-floating configuration

In the free-floating configuration all six samples were successfully tested. The unlock and release sequence remained the same as performed during testing in rack-bound configuration. At the start of each test run, the BionicWingSat was released by the operator hovering in the free-floating area during the 0g-phase. While freely floating the doors were unlocked and open followed by the wing release about 2 s later. As soon as the wings were released the BionicWingSat started rotating about its z-axis deploying its wings. On several parabolas, the residual g-vectors during the 0g-phase led the BionicWingSat to drift into the net of the free-floating area before the wings were able to flatten out completely. The complete deployment process is depicted in the sequence of images shown in in Fig. 30.

When analyzing the onboard data of the gyroscope of the BionicWingSats, the rotating behavior becomes also apparent, as shown in the plots of the angular acceleration α_z of the BionicWingSat about its z-axis is plotted over time of Fig. 31. As before, the angle of the servo motor of the release mechanism is plotted in order to identify the associated event of the unlock and release sequence. One can observe that the angular acceleration starts, with decreasing negative angular acceleration, about the BionicWingSat z-axis at mark ③, as soon as the wing release was initiated and the wings start to unfurl. The peak angular rotation (minimum), α_{zMin} , was reached in the middle of the self-deploying process of the wings at about three seconds. This behavior can be observed for all wing types and parabolas in the free-floating configuration. After a peak negative angular acceleration is an acceleration in the opposite direction until reaching an almost steady state with a quasi-constant angular velocity. This visible reduction of angular acceleration after achieving the handling state at mark ⑥ at about 110° servo angle can be attributed to the BionicWingSat drifting into the surrounding net, due to residual g-vectors, and to the retraction of the safety leash by the operator. In parabolas #2, #7, #21 and #23 an unfurling wing wiped across the rubberlike elastic safety bumpers of a door and resulted in a rotation of the wing itself, that lead to a disturbed deployment and to possible further dynamics of the BionicWingSat.

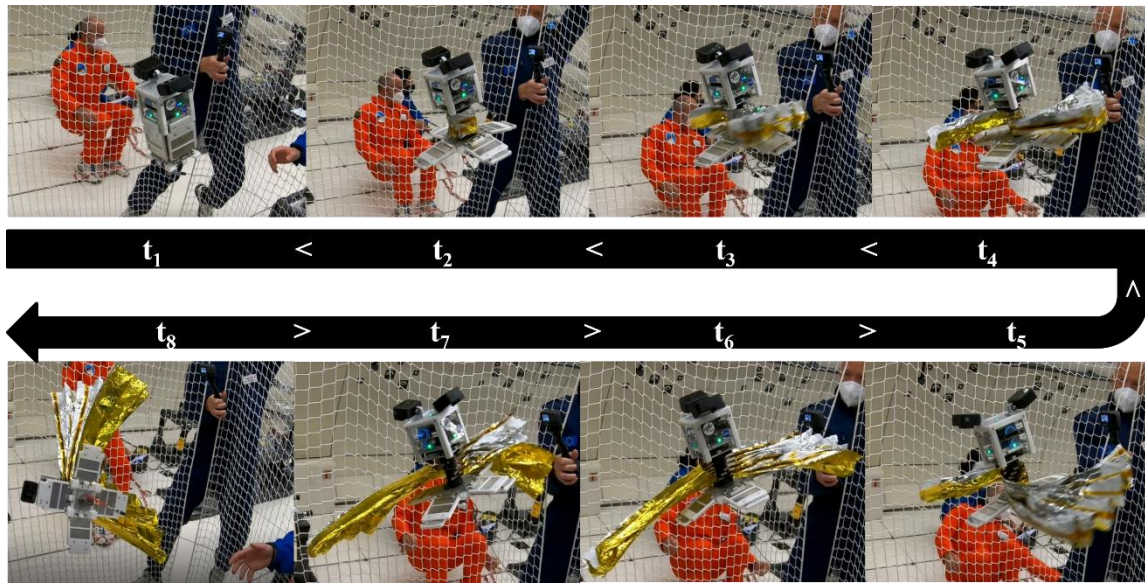


Fig. 30. Time lapse free-floating BionicWingSat.

The analyzed data for this test configuration is summarized in Table 3. Here the values for the angular acceleration at its peak at α_{zMin} are in the same range from -212.4 rad/s^2 to -272.4 rad/s^2 over all test wing types. Additionally, these peaks all occur at almost the same time, approximately 3000 ms after the normalized start of recording (normalized to 1000 ms before door opening is initiated at mark ①).

When comparing results within one wing sample type, the three samples of the D-I2-I5-iv wing type produce very similar values with a minimum angular acceleration α_{zMin} of $-212.4 \text{ rad/s}^2 \sim -240.8 \text{ rad/s}^2 \sim -229.4 \text{ rad/s}^2$. This and the time of occurrence of the peak indicate a good repeatability as one can observe in Table 3. The two samples of the wing type D-I2-I5 with values for α_{zMin} of $-272.4 \text{ rad/s}^2 \sim -268.9 \text{ rad/s}^2$ also exhibited peak acceleration times.

Of the three different sample wing types, wing type D-I2-I5 produces the highest angular accelerations, followed by wing type N-I2-I5-iv and lastly wing type D-I2-I5-iv. Although the wing types N-I2-I5-iv and D-I2-I5-iv feature an identical design, the difference in angular acceleration can be attributed to the different build material of the hinge assemblies, thus generating different deployment forces and moments.

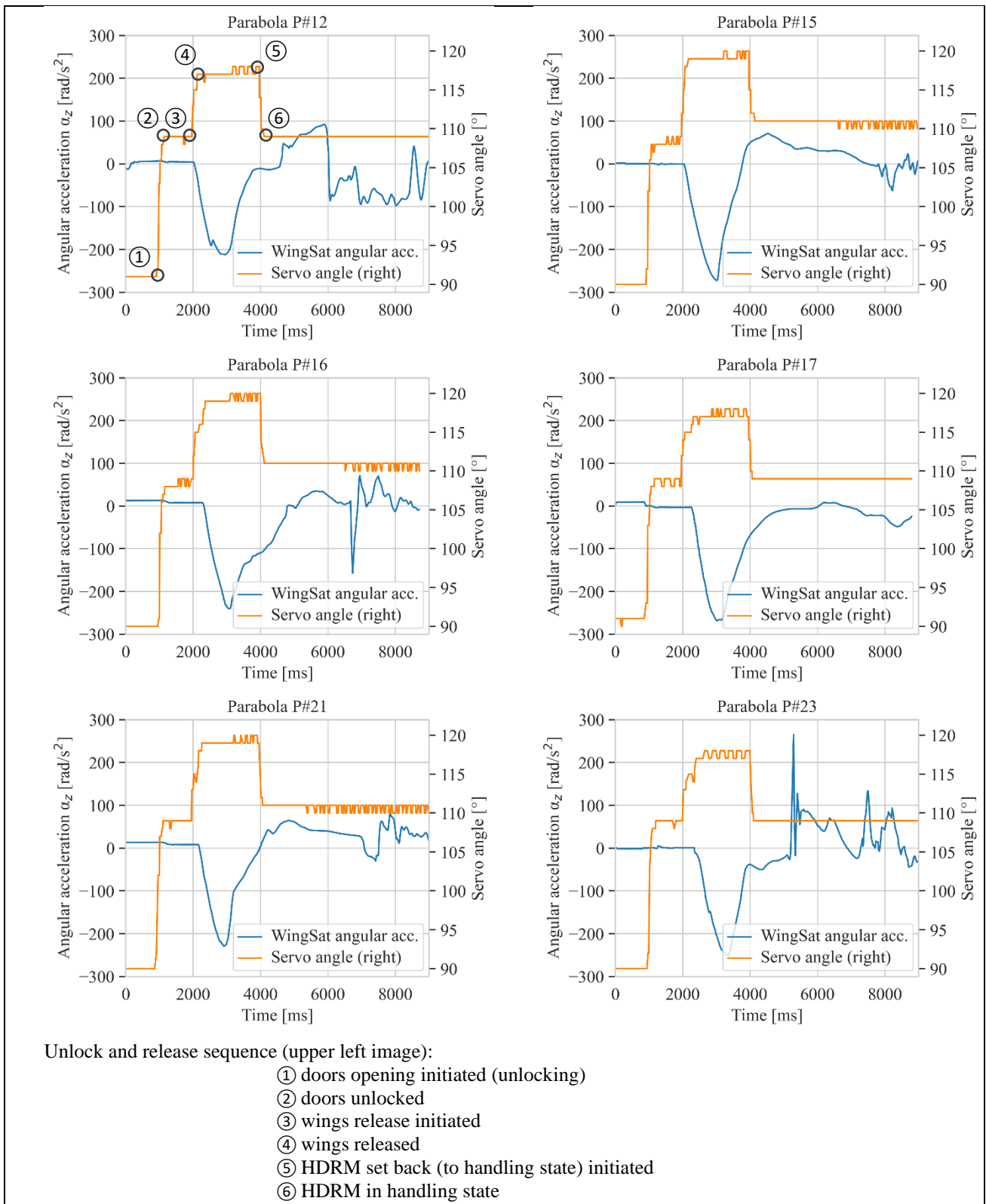


Fig. 31. Angular acceleration of BionicWingSat during free-floating deployment tests.

Cameras had originally been intended for use in measuring the flatness of the deployed wings but proved not to be useful during the microgravity tests. Nevertheless, the video footage provided images, as presented in Fig. 32, for a qualitative assessment of flatness. Residual accelerations induced motion throughout the free-flying tests however, and several samples ran into the safety nets, making it difficult to even give a qualitative assessment of which wing type was most flat at the point of full deployment. For all wings, creep in the hinge materials residual plastic deformations seemed

to be the main driver for not achieving the original flatness they had during manufacturing, as one can observe in the images of Fig. 32.

Table 3. Minimum angular accelerations of free-floating BionicWingSat during wing deployment.

<i>Parabola</i>	<i>Wing sample type</i>	t_{Min} [ms]	α_{zMin} [rad/s ²]	δ_{azMin} [°]
P#12	D-I2-I5-iv	2950	-212.4	117
P#15	D-I2-I5	3010	-272.4	119
P#16	D-I2-I5-iv	3080	-240.8	119
P#17	D-I2-I5	3020	-268.9	118
P#21	D-I2-I5-iv	2910	-229.4	119
P#23	N-I2-I5-iv	3340	-250.7	117

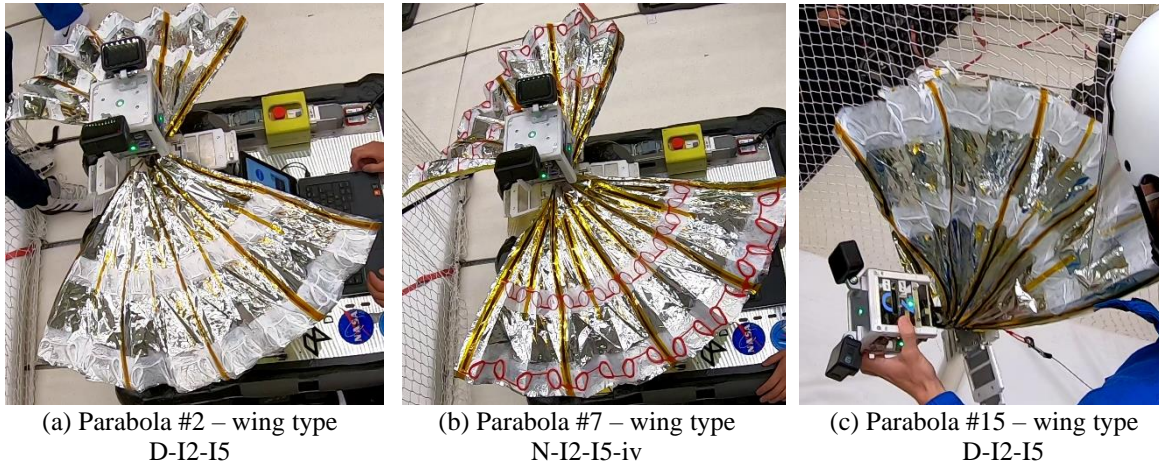


Fig. 32 Deployed wings in rack-bound and free-floating configurations.

VI. Conclusion

In this paper, a design for a biologically inspired and structurally integrated drag sail membrane is developed and tested in microgravity. Different types of hinge elements were investigated with a type of O-hinge identified as the most promising. After investigating many materials, combinations of materials, and various ALM machines, Nylon material delivered through a fused deposition process was chosen to produce samples for microgravity experiments. Ground testing and later experiments in microgravity show that while the wing concept is functional, many aspects of the vision of self-deploying integrated structures still need to be improved. Microgravity testing showed that the hinge structures that were capable of self-deploying at a subscale on the ground were incapable of doing this in the short period of time available. It is possible that in space, such structures would finish deploying but in the parabolic flight where microgravity is immediately followed by a period of high gravity, this could not be shown. Further investigation into creep resistance is needed to solve this problem or else a more energetic structure capable of fully deploying in a short time period must be used.

During microgravity testing, several observations were made that were backed up by measured data. First, despite damping, the opening of the doors imparted measurable force on the rest of the satellite, meaning that in free flight it would induce motion. In free-flight, video and accelerometer data document that the deployment of the doors induced translational motion while the deployment of the wings consistently produced angular acceleration about the z-axis of the vehicle. Different types of wings were shown to produce different amounts of angular acceleration as they unfurled. That the highest acceleration values come from wing type D-I2-I5 generated came at a surprise, as the intermediate radial stiffener is thought to increase deployment forces and improve flatness. However, since additional elements on a wing are a trade-off between deployment forces by stored strain energy and additional fold lines coupled with an increase of friction when unfolding, the higher values for D-I2-I5 are assumed to have its origin in lower friction forces to be overcome when deploying. Moreover, some design features led to effects that were not observed in previous ground testing under gravity. For example did the safety bumpers, introduced late in the design process, cause the wings to rotate unintentionally and flip during the

deployment process as the doors were apparently not moved out of the way to the necessary degree, thus disturbing a free deployment for some instances.

Testing in microgravity on a parabolic flight proved more challenging for this structure than expected. In the rack-mounted configuration, vibrations from the plane's engines were transmitted through the floor, exciting the BioWingSat and saturating any acceleration measurements. Pre-flight analysis of the dynamics of the rack and CubeSat system might have identified this as a risk. In free flight, the tiny amounts of remaining acceleration in microgravity caused the BioWingSat to coast into the netting walls, ruining some data and making it hard to judge wing flatness during several tests. A larger enclosure would have given the wings more time to deploy but with residual creep still present in the deployed structures, the parabolas still did not provide enough time to see if the wings would return to being flat in true microgravity. Knowing this, future tests should be limited to structures that deploy more quickly or which can be gravity offloaded between parabolas to allow continued deployment when microgravity returns.

The work presented in this paper is envisioned as a step in a longer process of developing self-deploying membrane structure. Future research could choose to address these aspects individually, improving wing design for packing efficiency with material for space with low creep tendencies, looking for a manufacturing method that truly integrates the structure into the membrane without adhesive, and finding a way to reproduce these results with space-rated materials.

Acknowledgments

This research has been carried out under an Implementing Arrangement between the National Aeronautics and Space Administration and the German Aerospace Center for Cooperative Research on Deployable Composite Booms.

The authors would like to thank DLR Space Research and Technology directorate and its former chair Prof. Dr. Hans-Jörg Dittus, the DLR institute director Professor Martin Wiedemann, as well as the head of DLR Department of Composite Design Prof. Dr. Christian Hühne for funding and supporting the microgravity test campaign. Moreover, the authors would like to acknowledge the support of the NASA Space Technology Mission Directorate Game-Changing Development Deployable Composite Booms project, the NASA Langley Research Center, Structural Dynamics Branch, Dr. Martin Annett, and Dr. Keith Belvin, Dr. Olive Stohlman and Dr. Jin Ho Kang provided value advice on adhesion strategies. This work would not have been possible without the tireless efforts, ingenuity, and curiosity of NASA interns Ms. Amy Caldwell and Ms. Danielle DaCosta.

References

- [1] Belvin, Zander et al., U.S. Provisional Patent Application for "Manufacturing of Low Mass, Large-Scale Hierarchical Thin Film Structural Systems," No. 61/431,245, filed on January 10, 2011.
- [2] Belvin, W. K., Zander, M. E., Sleight, D. W., Connell, J., Holloway, N., and Palmierix, F., "Materials, Structures and Manufacturing: An Integrated Approach to Develop Expandable Structures," in *53rd AIAA/ASME/ASCE/AHS/ASC Structures, Structural Dynamics, and Materials Conference*, Waikiki, Honolulu, Hawaii, 2012, AIAA 2012-1951.
- [3] Zander, M. E. and Belvin W. K., "Concept-Development of a Structure Supported membrane for Deployable Space Applications – From Nature to Manufacture and Testing," in *European Conference of Spacecraft Structures, Materials & Environmental Testing*, Noordwijk, The Netherlands, 2012.
- [4] Foust, J., "FCC to Set Five Year Deadline for Deorbiting LEO Satellites," *Space News*, 8 Sept, 2022, <https://spacenews.com/fcc-to-set-five-year-deadline-for-deorbiting-leo-satellites/>, Accessed on 5 December, 2022.
- [5] Zander, M.E., "Development of a Structure supported Membrane for deployable Space Applications", Diploma Thesis, 2010.
- [6] Haas, F.; Gorb, S., and Wootton, R.J., "Elastic Joints in Dermapteran Hind Wings: Materials and Wing Folding," in: *Arthropod Structure & Development*, Vol.29, p. 137-146, Elsevier Science Ltd., 2000.
- [7] Faber, J. A., Arrieta, A. F., and Studart, A. R., "Bioinspired Spring Origami," *Science*. DOI: <https://doi.org/10.1126/science.aap7753>, 2018, p. 1386–1391.
- [8] Brady, T. K. and Sweeney, D. J., "International Space Station (ISS) Solar Array Wing (SAW) Lessons Learned," NASA TM-2011-217064, Vols. 1 & 2, March 2011.
- [9] Banik, J.A., and Hausgen, P., "Roll-Out Solar Arrays (ROSA): Next Generation Flexible Solar Array Technology for DoD Spacecraft," *2017 AIAA SPACE and Astronautics Forum and Exposition*, 12-14 September 2017, Orlando, Florida. AIAA-2017-5307.
- [10] Murphy, M., Eskenazi, M.I., McEachen, M.E., and Spink, J.W., "UltraFlex and MegaFlex – Advancements in Highly Scalable Solar Power," *3rd AIAA Spacecraft Structures Conference*, 4-8 January, 2016, San Diego, CA, AIAA-2016-1947.
- [11] Johnson, C. L., Carr, J., Fabisinski, L., Russell, T., and Smith, L., "Lightweight Integrated Solar Array (LISA): Providing Higher Power to Small Spacecraft," in *13th International Energy Conversion Engineering Conference, AIAA Propulsion and Energy Forum*, (AIAA 2015-3896), 2015.
- [12] Alhorn, D.C., Casas, J.P., Agasid, E.F., Adams, C.L., Laue, G., Kitts, C., and S. O'Brien, "NanoSail-D: The Small Satellite That Could!," 25th Annual AIAA/USU Conference on Small Satellites, Logan, August, 2011, UT, SSC11-VI-1.
- [13] Spencer, D., Betts, B., Bellardo, J., Diaz, A., Plante, B., and Mansell, J., "The LightSail 2 Solar Sailing Technology Demonstration," *Advances in Space Research (ASR)*, Vol. 67, Issue 9, pp. 2878-2889.

- [14] Lockett, T.R., Castillo-Roger, J., Johnson, L., Matus, J. Lightholder, J., Marinan, A., and Few, A., "Near-Earth Asteroid Scout Flight Mission," in *IEEE Aerospace and Electronic Systems Magazine*, vol. 35, no. 3, pp. 20-29, 1 March 2020.
- [15] Wilkie, W.K., Fernandez, J.F., Stohlman, O.R., Schneider, N.R., Dean, G.D., Kang, J.H., Warren, J.E., Cook, S.M., Brown, P.L., Denkinds, T.D., Horner, S.D., Tapio, E.D., Straubel, M., Richter, M., and Heiligers, J., "An Overview of the NASA Advanced Composite Solar Sail (ACS3) Technology Demonstration Project," *AIAA SciTech Forum*, 11–15 & 19–21 January 2021, VIRTUAL EVENT, AIAA 2021-1260.
- [16] Johnson, L., Everett, J., McKenzie, D., Tyler, D., Wallace, D., Wilson, J., Newmark, J., Turse, D., Cannella, M., and Feldman, M., "The NASA Solar Cruiser Mission – Solar Sail Propulsion Enabling Heliophysics Missions," *36th Annual Small Satellite Conference*, Logan, UT, 6-11 August, 2022, SSC22-II-03
- [17] Mori O, Shirasawa Y, Mimasu Y et al., "Overview of IKAROS Mission: Part I Flight Programs," Macdonald M (ed) *Advances in Solar Sailing*. Springer, pp. 25–43, 2014.
- [18] Sawada, H., Mori, O., Okuizumi, N., Shirasawa, Y., Miyazaki, Y., Natori, M., Matunaga, S., Furuya, H., and Sakamoto, H., "Mission Report on The Solar Power Sail Deployment Demonstration of IKAROS," *52nd AIAA/ASME/ASCE/AHS/ASC Structures, Structural Dynamics and Materials Conference*, 4-7 April, 2011, Denver, CO, AIAA 2011-1887.
- [19] Stohlman, O., Fernandez, J.M., Lappas, V., Hillebrandt, M., Hühne, C., and Straubel, M., "Testing of the DeorbitSail Drag Sail Subsystem," *54th AIAA/ASME/ASCE/AHS/ASC Structures, Structural Dynamics, and Materials Conference*, April 8-11, 2013, Boston, MA, AIAA 2013-1907
- [20] Davis, B., Tomcheck, A., Turse, D., VanHalle, R., Medina, K., Francis, W., and Pearson, C., "Development of a High Strain Composite Tip-Rolled De-Orbit Sail; Technology Review and Story of Flight Integration," *AIAA SciTech Forum*, 7-11 January 2019, San Diego, CA, AIAA 2019-1750.
- [21] Ewing, A.P., Back, J.M., Schuettpelez, B.M., and Laue, G.P., "James Webb Space Telescope Sunshield Membrane Assembly," *50th AIAA/ASME/ASCE/AHS/ASC Structures, Structural Dynamics, and Materials Conference*, 4-7 may, 2009, Palm Springs, CA, AIAA 2009-2156